Correlated static atomic displacements and transmission-electron-microscopy contrast in compositionally homogeneous disordered alloys

Frank Glas
France Telecom, Centre National d'Etudes des Télécommunications, Paris B, Laboratoire de Bagneux, 196 avenue Henri Ravéra, Boîte Postale 107, 92225 Bagneux Cedex, France
(Received 2 May 1994)

We investigate several consequences of the atomic size effect in crystalline III-V alloys by performing numerical calculations in the framework of the extended valence-force-field model and we compare our results with available experimental data. First, we demonstrate the existence in these alloys, even if they are fully disordered, of large anisotropic spatial correlations between the static atomic displacements from the sites of the average sublattices, and we calculate the corresponding correlation functions. Second, we show that these very correlations induce a previously unrecognized characteristic contrast in the conventional transmission-electron-microscopy images of such alloys. We explore the behavior of this atomic-size-effect contrast upon changing the diffraction conditions. These results are obtained by simulating large alloy supercells and by subsequently performing dynamical image calculations. Finally we compare qualitatively and quantitatively our calculated contrast with the fine-scale contrasts observed in the experimental micrographs of these alloys.

I. INTRODUCTION

A. The atomic size effect in fully disordered alloys

When atoms having different covalent or ionic radii are present in a totally or partially disordered crystalline alloy, static atomic displacements (SD's) from the sites of the average lattice or sublattice shared by these atoms usually exist. The various consequences of these SD's are termed atomic size effects (ASE's). We define as compositionally homogeneous or fully disordered an alloy where there is no correlation at all between the occupations by the various atomic species of the sites of the shared lattice or sublattice(s). In such an alloy, deviations from spatial chemical uniformity still inevitably exist, but only at the atomic level; they result solely from the uncorrelated statistical fluctuations in the distribution of these species. If the alloy is not fully disordered (whether this is due to ordering or clustering), the SD's are, of course, also spatially correlated, although the correlation functions of the compositional and displacement disorders need not be related in any simple way (unless ordering is perfect). It has, however, been recognized long ago that, even in the case of total substitutional disorder, the SD's may be correlated, at least over short distances; this gives rise to the well-known size-effect modulation of the diffuse background observed in the x-ray-diffraction patterns of such alloys.[1] Nevertheless, most studies so far have dealt with alloys where spatial correlations of the site occupations and of the SD's are both present. In particular, the interpretation of the diffraction data has been mainly concerned with separating the diffuse contribution of the SD's from that of the correlations of occupations, in order to evaluate the latter accurately.[1,2]

However, a renewed interest in the ASE's in fully disordered alloys recently arose. We recognized the presence of strikingly anisotropic features in the electron and x-ray diffuse scattering patterns of some III-V ternary and quaternary alloys.[3] Most of these alloys display ASE's, which will be described in more detail in Sec. II. The peculiar diffuse features consist of pairs of satellite planes passing away from the main diffraction spots and separated by a gap of intensity. Since electron-beam x-ray microanalysis had failed to prove the presence of proper small-scale composition inhomogeneities in the samples studied[4] and since no model of local order or composition variation compatible with the experiments could be found, we tried to interpret these features by simulating the diffuse scattering patterns expected from totally disordered homogeneous III-V alloys.[5] Our simulations reproduced the diffuse planes very well. We concluded that the latter could be due to the anisotropic spatial correlations of SD's in a fully disordered alloy.[5] We obtained the SD's in our simulated random alloys by using the valence-force-field (VFF) model of Keating[6] and Martin[7] extended to the III-V alloys by Podgórny *et al.*[8] This model, which takes fully into account the tetrahedral coordination characteristic of the sphalerite structure of the III-V alloys and considers both bond-stretching forces between nearest-neighbor (NN) atoms and bending forces between bonds sharing a common atom, had previously given other results in excellent agreement with the experiments (see Sec. II). Independently, Butler, Withers, and Welberry noticed the same kind of diffuse features in the x-ray-diffraction patterns of some oxide alloys and also interpreted them in terms of correlated SD's in a fully disordered alloy.[9] Indeed, these authors clearly identified the contributions to the diffraction patterns of the SD correlations along various directions and at several distances. On the other hand, in their numerical simulations they only considered a simplified two-dimensional square lattice with only bond-stretching forces between NN's.

B. Transmission-electron-microscopy contrast and specimen compositional homogeneity

The existence of such anisotropic spatial correlations of SD's in fully disordered alloys raises the question of their effect in transmission electron microscopy (TEM). It is generally admitted that any contrast which may be observed in the conventional TEM (CTEM, as opposed to high-resolution TEM) micrographs of uniformly thin and unbent crystalline specimens results from some spatial nonuniformity of these specimens. One usually distinguishes broadly between structure-factor contrast and strain contrast.[10] The former is due to the direct effect of the chemical or structural inhomogeneities on the structure factors of the transmitted and diffracted beams contributing to the electron wave function, whereas the latter results from the change of diffraction conditions caused by the strain fields induced in their vicinity by such inhomogeneities or by lattice defects. Conversely, it is believed that a defect-free homogeneous specimen (uniformly thick and uniformly oriented with respect to the incident beam) should display no contrast. However, SD's constitute a microscopic strain, and, provided they are large enough and spatially correlated, they should also induce some TEM contrast. Indeed, we will show in this paper that, contrary to the above-mentioned assumption, because of the correlated SD's, alloys with ASE's may display considerable TEM contrast, even if they are ideally homogeneous in composition.

In the particular case of the III-V alloys with ASE's, a characteristic fine granular contrast is observed in the CTEM micrographs of all epitaxial layers.[3,4,11–18] Most authors assume that this contrast proves that these layers are always inhomogeneous in composition. This is partially based on analogies, which do not resist a detailed examination of the behavior of the contrast upon changing diffraction conditions,[4,16] with the contrasts observed in some metallic alloys which do undergo spinodal decomposition or phase separation.[19] On the contrary, we suggested earlier that, because of the SD's, the fine contrast might well be compatible with compositional homogeneity.[4] This question can now be reexamined in the light of the image calculations here reported.

C. Contents

Our aim is twofold. First, we give quantitative values of the correlation functions of the SD's in compositionally homogeneous III-V alloys with ASE's. These results are obtained, for correlations along the major crystalline axes and for both longitudinal and transverse components of the SD's of the group-III and group-V atoms, by using the extended VFF model. Second, we demonstrate a previously unrecognized effect. Namely, we show that, somewhat surprisingly, compositionally homogeneous alloys may display considerable TEM contrast. We prove unambiguously that this contrast is caused by the SD's, and more precisely by the spatial correlations of the SD's. This effect, which is probably very general, is demonstrated here by performing dynamical image calculations for the same simulated specimens of III-V alloys with ASE's which provide the values of SD correlations. This demonstration has two major implications: (1) the almost universal belief that, in the absence of crystalline defects, CTEM contrast indicates compositional inhomogeneity is wrong (unless the meaning of "inhomogeneity" is extended to encompass the purely uncorrelated fluctuations in site occupations); (2) the interpretation of the observation of the fine-scale TEM contrast as a proof that all the epitaxial layers of III-V alloys with ASE's are compositionally inhomogeneous has to be reexamined critically.

In Sec. II, we describe the VFF calculations whose results are later used to determine both the spatial correlations of SD's and the induced TEM contrast. In Sec. III, we give and discuss the values of the major SD correlation functions for a III-V alloy with ASE's. Section IV describes the calculation of the TEM contrast in an alloy with SD's; although the details refer specifically to the III-V alloys, the method and the discussion are general. In Sec. V, we present the results of such TEM simulations performed for compositionally homogeneous III-V alloys, namely, images and an analysis of their statistics. In Sec. VI, we analyze the various possible sources of the large contrast that these simulated micrographs display and demonstrate that it is indeed induced by the spatial correlations of SD's investigated in Sec. III. Finally, we discuss in Sec. VII the implications of these simulations for the interpretation of the experimental TEM micrographs of these alloys.

II. THE STATIC ATOMIC DISPLACEMENTS IN SIMULATED DISORDERED CRYSTALS OF III-V ALLOYS

To investigate both the SD correlations and the induced TEM contrast, we simulate very large crystals of fully disordered ternary $A_xB_{1-x}C$ III-V alloys. In these alloys, either the group-III or the group-V sublattice (termed "mixed") of the sphalerite structure hosts two types of atoms.[20] In all cases, except when Ga and Al share the group-III sublattice, the atoms of the mixed sublattice have covalent radii differing by several percent[20] and ASE's occur. ASE's are also present in the quaternary $A_xB_{1-x}C_yD_{1-y}$ alloys, which possess two mixed sublattices, and we expect our results to apply to these alloys as well.

A convenient starting point to describe the III-V alloys is the virtual crystal approximation (VCA),[20] which consists in three assumptions: the crystal has a perfect cubic sphalerite lattice (A1) whose parameter follows Vegard's law (A2) and whose sites are occupied by "average" atoms (A3). There is one type of average atom per sublattice. According to (A2), its covalent radius varies linearly with the atomic concentration on this sublattice: in $A_xB_{1-x}C$, the (A,B)-sublattice average covalent radius varies with x between those of A and B, the C-sublattice "average" remaining, of course, equal to the covalent radius of C.

The occurrence of ASE's in these alloys has been proven by several experiments. Extended x-ray-absorption fine structure (EXAFS) has shown, first for $In_xGa_{1-x}As$,[21,22] and subsequently for many other III-V

alloys,[23] that the distance between two nearest-neighbor atoms (belonging to the two different sublattices) tends to remain equal, for any composition, to the sum of their actual covalent radii; thus, it differs from the VCA value, which is the composition-dependent sum of the group-III and group-V average covalent radii. Since, however, diffraction proves the existence of an average lattice whose parameter follows Vegard's law, and which can thus be considered as the VCA lattice, considerable SD's from the sites of this lattice must exist. Our previous study of the characteristic distribution of diffusely scattered intensity found in the electron- and x-ray-diffraction patterns of these alloys confirmed the existence of the SD's.[5] Indeed, the agreement was very good between the experimental patterns and those calculated by applying the kinematical diffraction theory to large simulated crystals for which the SD field had been found by using the extended VFF model (see Sec. I A and details below). This model also provides distributions of NN distances in good agreement with EXAFS,[8,5] and values of the alloy mixing enthalpy corresponding to the measured ones.[8] In conclusion, two of the VCA assumptions are invalid: (A1) because of the SD's from the sites of the average lattice and (A3) because average atoms obviously do not exist.

We now indicate briefly how the extended VFF model yields the SD fields used in the rest of this paper. In what follows, reference is to the perfect simple cubic virtual crystal (VC), with four group-III and four group-V sites (index n, position $\mathbf{r}_n$) per unit cell of side a. The simulated crystals are $In_{0.5}Ga_{0.5}As$ supercells containing 6.48×10^6 atoms distributed in $N_X=N_Y=60$ unit cells along $\mathbf{X}=[001]$ and $\mathbf{Y}=[010]$ and $N_Z=225$ unit cells along $\mathbf{Z}=[001]$; since $a\sim0.586$ nm, their dimensions are thus $35\times35\times132$ nm^3. This large number of cells along $\mathbf{Z}$ will be needed in Sec. IV in order to simulate typical thicknesses of CTEM specimens. The SD's were calculated as described previously for rhombohedric supercells.[5] In order to simulate compositionally homogeneous crystals, the nature (In or Ga) of the atom present at each site of the mixed group-III sublattice was first drawn without any correlation between the occupation of the sites (no ordering or clustering), the group-V sublattice being entirely populated by As. All atoms were then displaced in the vicinity of their sites without being allowed to exchange sites. The process was iterated until less than 0.1% of the atoms had moved by more than 0.5 pm with respect to their previous positions.

The equilibrium SD's $\mathbf{R}(\mathbf{r}_n)$ were obtained by minimizing the strain energy given, in the extended VFF model, as a function of all the actual atomic positions $\mathbf{r}_n+\mathbf{R}(\mathbf{r}_n)$ by

$$U=\tfrac{1}{4}\sum_n\sum_m\tfrac{3}{4}\alpha_{nm}(d_{nm}^2-d_{0,nm}^2)^2/d_{0,nm}^2+\tfrac{1}{4}\sum_n\sum_{\substack{m,m'\\ m\neq m'}}\tfrac{3}{4}\beta_{nmm'}(\mathbf{d}_{nm}\cdot\mathbf{d}_{nm'}-d_{0,nm}d_{0,nm'}\cos\theta_{0,nmm'})^2/d_{0,nm}d_{0,nm'}\ . \tag{1}$$

In (1), n describes all the atomic sites, m and m' the four NN sites of n,

$$\mathbf{d}_{nm}=[\mathbf{r}_m+\mathbf{R}(\mathbf{r}_m)]-[\mathbf{r}_n+\mathbf{R}(\mathbf{r}_n)]$$

is the vector of length d_{nm} joining in the actual alloy the atoms belonging to (but displaced from) sites n and m, $d_{0,nm}$ is the corresponding length in the binary compound constituted of those atoms occupying sites n and m, and $\theta_{0,nmm'}$ is the equilibrium bond angle which, as shown by previous simulations,[8] must be chosen as the perfect tetrahedron angle; α_{nm} and $\beta_{nmm'}$ are the bond-stretching and bond-bending constants,[6–8] depending on the atomic species present at sites n,m, and m'. The equilibrium SD field is obtained by minimizing U. Periodic boundary conditions (PBC's) were applied along $\mathbf{X}$ and $\mathbf{Y}$, but not always along $\mathbf{Z}$. In the case of the image calculations, where $\mathbf{Z}$ is taken as the direction along which the TEM specimen is thin and the fast electrons travel (see Sec. IV), elastic relaxation at the free surfaces could thus be taken into account simply but rather crudely by omitting in (1) the terms involving the cut bonds, which connect the top and bottom of the specimen in the full PBC scheme.

Three compositionally homogeneous fully disordered crystals were simulated in order to eliminate possible artifacts associated with any particular random distribution of the atomic species on the mixed sublattice. Only features observed for all specimens will be discussed. Many smaller specimens were also simulated.

III. CORRELATION FUNCTIONS OF THE STATIC ATOMIC DISPLACEMENTS IN COMPOSTIONALLY HOMOGENEOUS DISORDERED III-V ALLOYS

In these disordered alloys, the spatial correlations between the SD's are best described in terms of the sublattice displacement pair correlation functions (DPCF's) along direction $\boldsymbol{\alpha}$ of the components of the SD's along direction $\boldsymbol{\beta}$, which we define as

$$F_{\alpha,\beta}^{I,J}(r)=\langle R_\beta(\mathbf{r}_p)R_\beta(\mathbf{r}_p+r\boldsymbol{\alpha}')\rangle\ , \tag{2}$$

where the VC sites at $\mathbf{r}_p$ and $\mathbf{r}_p+r\boldsymbol{\alpha}'$ belong, respectively, to sublattices I and J, $\boldsymbol{\alpha}$ and $\boldsymbol{\beta}$ are two crystal axes, $\boldsymbol{\alpha}'$ is a unit vector along $\boldsymbol{\alpha}$, and $R_\beta(\mathbf{r}_p)$ is the component along $\boldsymbol{\beta}$ of the SD at VC site $\mathbf{r}_p$; the angular brackets denote the average, for r fixed, over all sites p of sublattice I. Such functions are of course defined only if r is a VC intersite distance along $\boldsymbol{\alpha}$.

Figure 1 gives the correlation functions of the longitudinal and transverse SD's for three dense correlation directions $\boldsymbol{\alpha}$: $\langle110\rangle$, $\langle100\rangle$, and $\langle111\rangle$. Starting from a given central atom p, one may find along $\boldsymbol{\alpha}$ either only atoms belonging to the same sublattice ($I=J$; case of $\langle110\rangle$ and $\langle100\rangle$) or atoms belonging alternatively to both sublattices ($I\neq J$ is allowed; case of $\langle111\rangle$). Note that, in order to show with enough detail in a single diagram the variations at low and high r of the DPCF's, we display the square roots of their moduli, multiplied by the

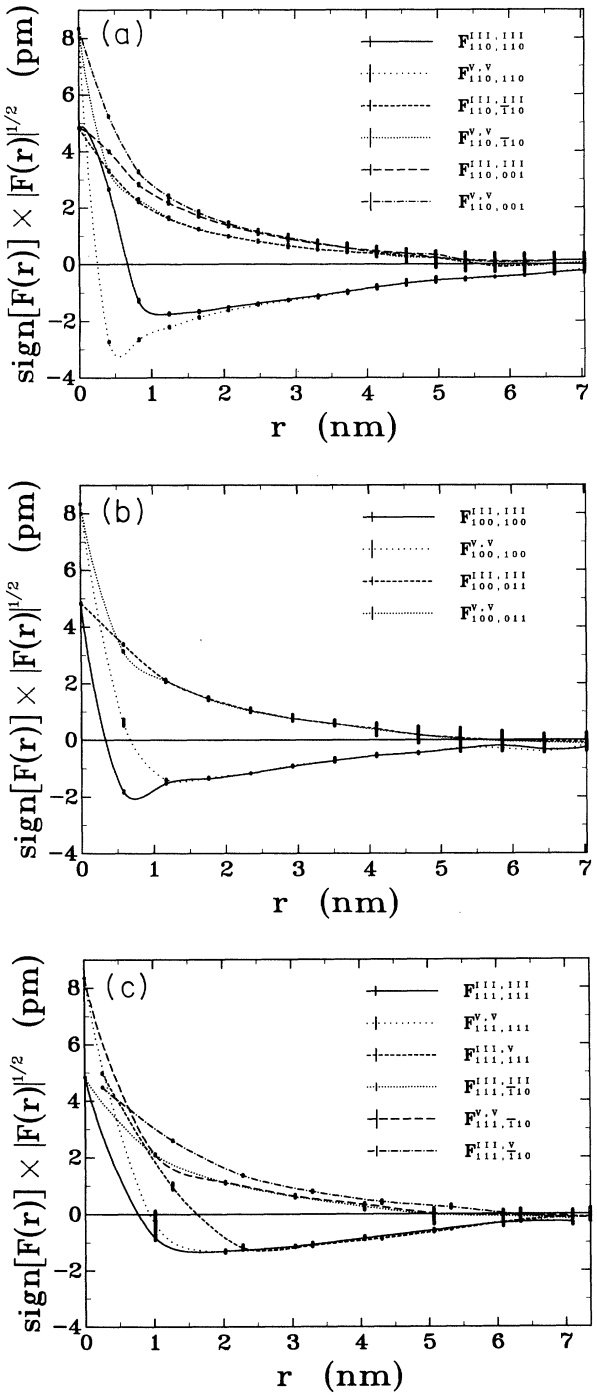

FIG. 1. Calculated displacement pair correlation functions $F^{I,J}_{\alpha,\beta}$ for correlation directions $\alpha=\langle 110\rangle$ (a), $\langle 100\rangle$ (b), and $\langle 111\rangle$ (c), and for longitudinal [first two curves in (a) and (b), first three curves in (c)] and transverse (the other curves) components of the SD's. The curves are fits to the averages over the three simulated specimens, and the thick vertical segments give the spread of the data. The thin vertical segments in the keys give the largest values of the square roots of the moduli of the DPCF's (over the spatial range studied) for the same specimens with randomized displacements (see text). For $\alpha=\langle 100\rangle$, the DPCF's for $\beta=\langle 010\rangle$ are very close to those for $\beta=\langle 011\rangle$.

sign (± 1) of the DPCF (to preserve the difference between correlations and anticorrelations).

The main conclusions are the following.

(i) There exist strong correlations between the SD's, extending over a range long with respect to the interatomic distances. As expected in our large but finite simulated crystals, the DPCF's never exactly vanish. To determine the range below which our calculation of nonzero DPCF's is surely relevant, we compare them (Fig. 1) with the DPCF's calculated for randomized specimens, where the same atoms, *each with its own SD,* have been randomly permuted between the VC sites; any spatial correlation between the SD's is then destroyed (except of course for $r=0$). This comparison proves that the correlations extend at least over 6, 5, and 4 nm along $\langle 110\rangle$, $\langle 100\rangle$, and $\langle 111\rangle$, respectively. To discover if even longer-range weak correlations exist, larger specimens should be considered. We check that the PBC's do not induce any artifact since the size of the present specimens is well above the ranges here determined. Finding the same value for the autocorrelation $F^{I,I}_{\alpha,\beta}(0)$ of any SD component for a given sublattice is a consequence of the cubic symmetry of the VC.

(ii) The DPCF's display two types of anisotropy. First, correlations between the transverse SD's are always positive, whereas correlations between longitudinal SD's are positive over a short range and then negative. The latter fact (already noticed by Butler, Withers, and Welberry[9] with their two-dimensional model) reflects the necessity to compensate any local translation of part of the crystal by a neighboring translation in the opposite sense. Secondly, correlations are more marked along $\langle 110\rangle$ than along $\langle 100\rangle$ or $\langle 111\rangle$; namely, they are larger for a given r and they extend further. This is because the $\langle 110\rangle$ directions are those of the chains of second nearest neighbors, joined by two $\langle 111\rangle$-oriented bonds; no such chains exist in the other directions. We demonstrate here our previous suggestion[5] that the observation in diffraction experiments of $\{110\}$-oriented diffuse reciprocal planes[3,5] is also a consequence of such a correlation anisotropy.

(iii) When r increases, well before the DPCF's vanish, $F^{III,III}_{\alpha,\beta}(r)$ and $F^{V,V}_{\alpha,\beta}(r)$ becomes nearly equal for given α and β, although the moduli of the SD's of the atoms of the pure V sublattice are on average larger than those of the mixed III sublattice.[8,24] This strongly suggests the existence of a medium-range strain field in these alloys fully homogeneous in composition. Indeed, that is what would be observed if each SD were the sum of a local average displacement $\bar{\mathbf{R}}$, independent of the sublattice, and of a complementary displacement, locally averaging to zero and depending on the nature of the atom and on the details of its close neighborhood only. Then, for distances larger than the size of the local averaging volume, the DPCF would reduce to the correlation function of the field $\bar{\mathbf{R}}$, independently of the sublattice. This can be checked, and an evaluation of what "local" means here can be obtained, by calculating the correlation functions of the SD's averaged over small volumes of increasing sizes, namely:

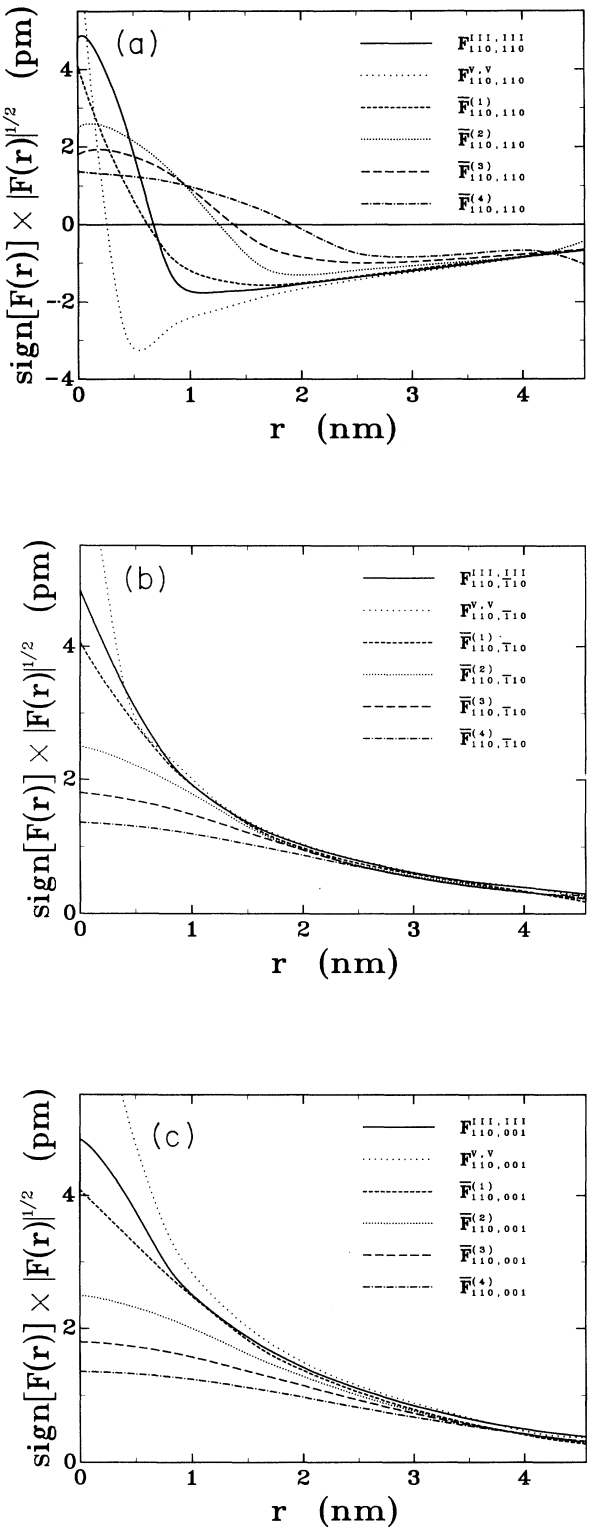

FIG. 2. Comparison of the displacement pair correlation functions with the correlation functions of the static displacements averaged over cubes containing 8, 27, 64, and 512 atoms, respectively. The correlation direction is $\alpha=\langle 110\rangle$ and the components of the displacements considered are along $\beta=\langle 110\rangle$ (a), $\langle \bar{1}10\rangle$ (b), and $\langle 001\rangle$ (c).

$$\bar{F}^{(n)}_{\alpha,\beta}(r)=\langle \bar{R}^{(n)}_{\beta}(\mathbf{r}_p)\bar{R}^{(n)}_{\beta}(\mathbf{r}_p+r\boldsymbol{\alpha}')\rangle \ , \tag{3}$$

where $\bar{R}^{(n)}_{\beta}(\mathbf{r}_p)$ is the component along $\boldsymbol{\beta}$ of the average displacement of all the atoms (group III and group V) contained in a cube of n^3 unit cells whose lower left corner (for instance) is at VC site $\mathbf{r}_p$. In Fig. 2, we compare these functions with the DPCF's, for $\boldsymbol{\alpha}=[110]$ and for one simulated specimen (similar conclusions were drawn for other directions and other specimens). We indeed observe that for large r, $\bar{F}^{(n)}_{\alpha,\beta}(r)$, $F^{\mathrm{III,III}}_{\alpha,\beta}(r)$, and $F^{\mathrm{V,V}}_{\alpha,\beta}(r)$ take the same values. For $n=1$ (average over eight atoms), this convergence is even obtained below 2 nm. Figure 2 also shows that $\bar{F}^{(n)}_{\alpha,\beta}(0)\neq 0$ even for n as large as 4 (average over 512 atoms), which indicates that the average SD in such large volumes still differs significantly from zero. This is yet another proof of the existence in these fully disordered specimens of a medium-range strain field.

IV. TEM IMAGE CALCULATION FOR A DISORDERED ALLOY WITH STATIC ATOMIC DISPLACEMENTS FROM AN AVERAGE LATTICE

Surprisingly, although only assumption (A2) of the VCA is valid (and indeed only for the average lattice), nearly all the TEM studies of the III-V alloys with ASE's have relied, if only implicitly, on the VCA, and, to our knowledge, none has taken the SD's into account. More generally, several reasons might explain why the contrast induced by the SD's in the TEM micrographs of concentrated alloys with ASE's has not yet been investigated. First, since its characteristic size may be of several nanometers (see Sec. V A), very large crystals have to be simulated, especially to reproduce the relatively high thicknesses pertaining to CTEM. Secondly, since in disordered crystals the SD's may vary rapidly from site to site, the usual CTEM "column approximation"[10] cannot be used *a priori*. Finally, most experimental work has been devoted to metallic alloys, where ordering or clustering often accompanies the SD's; the effect of the latter could thus not be isolated. The fundamental differences between the present work and the investigation of the effect on TEM micrographs of the SD's induced by *dilute* impurities will be discussed in Sec. VI C.

Although the details refer here to the III-V alloys with ASE's, the method described in this section is a general one to calculate the contrast induced by the SD's in simulated crystals. The specific features of the images of the III-V alloys will be discussed in the next section.

A. Computation of the elastic scattering potential of the disordered crystal

Calculating the images first requires calculating the potential responsible for the elastic scattering of the fast incident electrons in our simulated crystal. Once the strain energy U is minimized, we have all the necessary data, namely, the nature and exact position (average VC position plus SD) of all the atoms. Since the SD's are large and since the displacement field obtained from the VFF computation is not a continuous function of position but is defined only at the discrete lattice sites, we use the

rigid-ion approximation of the crystal potential,[25,26]

$$V(\mathbf{r})=\sum_n v_n[\mathbf{r}-\mathbf{r}_n-\mathbf{R}(\mathbf{r}_n)] , \tag{4}$$

where v_n is the potential of the atom attached to site n when placed at the origin. If e and m are the charge and relativistic mass of the electrons and h Planck's constant, we develop V as usual:

$$V(\mathbf{r})=(h^2/2me)\sum_g u_g(\mathbf{r})\exp(2\pi i\mathbf{g}\cdot\mathbf{r}) . \tag{5}$$

From (4) and (5), we have

$$u_g(\mathbf{r})=\int_{BZ} d\mathbf{k}\sum_n \hat{v}_n(\mathbf{g}+\mathbf{k}) \times\exp\{2\pi i\mathbf{k}\cdot[\mathbf{r}-\mathbf{r}_n-\mathbf{R}(\mathbf{r}_n)]\} \times\exp\{-2\pi i\mathbf{g}\cdot[\mathbf{r}_n+\mathbf{R}(\mathbf{r}_n)]\} , \tag{6}$$

where the Fourier transform $\hat{v}_n$ of v_n is defined by

$$\hat{v}_n(\mathbf{k})=(2me/h^2)\int_{RS} d\mathbf{r}\, v_n(\mathbf{r})\exp(-2\pi i\mathbf{k}\cdot\mathbf{r}) . \tag{7}$$

The integrals in (6) and (7) extend respectively over the VC first Brillouin zone (BZ) and full reciprocal space (RS). We index the atomic species Ga, In, and As by $q=1$, 2, and 3, respectively, and denote by $\hat{v}^q$ the three possible Fourier transforms defined by (7). We note that $\hat{v}^q(\mathbf{k})=f^q(k)/\pi$, where $f^q(k)$ is the scattering factor of atom q for electrons, which we take from Doyle and Turner.[27] We set $\sigma_n^q=1$ if site n is occupied by atom q, $\sigma_n^q=0$ if not. The components k_i of $|\mathbf{k}|$ in (6) are less than $1/(2a)$ and we find from our simulations that only about one SD component out of a thousand is larger than 0.022 nm; so $|2\pi k_i[\mathbf{R}(\mathbf{r}_n)]_i|\le 0.12$ and we can develop $\exp[-2\pi i\mathbf{k}\cdot\mathbf{R}(\mathbf{r}_n)]$ to the second order in $\mathbf{k}\cdot\mathbf{R}(\mathbf{r}_n)$. Thus

$$u_g(\mathbf{r})=\int_{BZ} d\mathbf{k}\exp(2\pi i\mathbf{k}\cdot\mathbf{r})\sum_{q=1}^{3}\hat{v}^q(\mathbf{g}+\mathbf{k}) \left[\sum_n \exp(-2\pi i\mathbf{k}\cdot\mathbf{r}_n)\sigma_n^q\exp\{-2\pi i\mathbf{g}\cdot[\mathbf{r}_n+\mathbf{R}(\mathbf{r}_n)]\}\right.$$
$$-2\pi i\sum_{i=1}^{3}k_i\sum_n \exp(-2\pi i\mathbf{k}\cdot\mathbf{r}_n)\sigma_n^q[\mathbf{R}(\mathbf{r}_n)]_i\exp\{-2\pi i\mathbf{g}\cdot[\mathbf{r}_n+\mathbf{R}(\mathbf{r}_n)]\}$$
$$-2\pi^2\sum_{i=1}^{3}\sum_{j=1}^{3}k_ik_j\sum_n \exp(-2\pi i\mathbf{k}\cdot\mathbf{r}_n)\sigma_n^q[\mathbf{R}(\mathbf{r}_n)]_i[\mathbf{R}(\mathbf{r}_n)]_j$$
$$\left.\times\exp\{-2\pi i\mathbf{g}\cdot[\mathbf{r}_n+\mathbf{R}(\mathbf{r}_n)]\}\right] . \tag{8}$$

Now, the sums over the sites n in (8) are simply Fourier sums which are easily computed, by using standard fast Fourier transform algorithms, for the set of $\mathbf{k}$ in the first BZ of components $k_i=n_i/N_ia$ $(i=X,Y,Z;-N_i/2\le n_i<N_i/2$ for N_i even); because of the PBC's, the sums vanish at any point not belonging to this fine reciprocal grid. It is then straightforward to calculate $u_g(\mathbf{r})$ and thus $V(\mathbf{r})$ from (5) and (6) at any required point in the supercell.

B. Computation of the TEM images

In the crystal, the TEM wave function Ψ corresponding to an incident plane wave $\exp(2\pi i\mathbf{K}\cdot\mathbf{r})$ of kinetic energy E_0 is projected on a set of plane waves, indexed by the VC reciprocal vectors $\mathbf{g}$ (the transmitted beam $\mathbf{g}=\mathbf{0}$ is always included). The current diffraction conditions are defined as usual[10] by the vectorial deviation parameters $\mathbf{s}_g$ measuring the deviation form the Bragg condition for $\mathbf{g}$:

$$\Psi(\mathbf{r})=\sum_g \phi_g(\mathbf{r})\exp[2\pi i(\mathbf{K}+\mathbf{g}+\mathbf{s}_g)\cdot\mathbf{r}] . \tag{9}$$

We suppose that $\mathbf{Z}=[001]$ is the normal to the TEM thin foil and we consider only incident primary beams of directions close to $\mathbf{Z}$. Then, only waves corresponding to vectors $\mathbf{g}$ in the (001) reciprocal plane are appreciably excited, the $\mathbf{s}_g$ are parallel to $\mathbf{Z}$, and we can use the dimensionless parameters $w_g=s_g\xi_g$, where, as indicated, reference is to the VC and ξ_g is the average extinction distance.[10] Moreover, we limit ourselves to conditions usually chosen for CTEM imaging near the Bragg condition for a given reflection $\mathbf{G}$, the so-called "systematic row" geometry:[10] $\mathbf{K}$ lies in the plane $(\mathbf{G},\mathbf{Z})$ and any $\mathbf{g}$ to be included in (9) is collinear to $\mathbf{G}$. The diffraction conditions are then fully defined by w_G. We include N beams (typically between two and eight) in the calculation.

Since the SD's are large and, despite their correlations, may vary rapidly between sites, we cannot *a priori* use the column approximation, which relies on a slow variation of the strain field in the directions normal to the beam. Instead, we follow the more rigorous treatment of Howie and Basinski[25] and Anstis and Cockayne.[26] We thus solve the following system of N equations:

$$\frac{\partial\phi_g}{\partial Z}=\pi i\sum_h\frac{1}{K}[u_{g-h}(\mathbf{r})+iu'_{g-h}(\mathbf{r})]\phi_h(\mathbf{r}) \times\exp[2\pi i(\mathbf{s}_h-\mathbf{s}_g)\cdot\mathbf{r}]-\frac{(\mathbf{K}+\mathbf{g})_X}{K_Z}\frac{\partial\phi_g}{\partial X}$$
$$-\frac{(\mathbf{K}+\mathbf{g})_Y}{K_Z}\frac{\partial\phi_g}{\partial Y}+\frac{i}{4\pi K_Z}\left[\frac{\partial^2\phi_g}{\partial X^2}+\frac{\partial^2\phi_g}{\partial Y^2}\right] , \tag{10}$$

where all derivatives are taken at $\mathbf{r}$ and $(\mathbf{K}+\mathbf{g})_i$ is the component of $(\mathbf{K}+\mathbf{g})$ along axis i ($\mathbf{X}$ or $\mathbf{Y}$). $u'_{\mathbf{g}}(\mathbf{r})$ is the imaginary part of the potential, which usually describes, for a perfect crystal, all the scattering out of the Bragg beams, the so-called absorption.[10] However, in the present case two kinds of absorption exist, which we treat differently. The first kind groups all the causes which exist even in a perfect crystal, the most important of which (and often the only one considered) being thermal diffuse scattering. Only this type of absorption is described by $u'_{\mathbf{g}}(\mathbf{r})$, which was taken as proportional to $u_{\mathbf{g}}(\mathbf{r})$, the ratio $u'_{\mathbf{g}}(\mathbf{r})/u_{\mathbf{g}}(\mathbf{r})$ depending on $\mathbf{g}$. The second type of absorption, due to scattering out of the VC Bragg beams by the SD's, is obviously taken into account by our full calculation of the diffuse intensity over the considered portion of reciprocal space.

Because in (6) the integral extends over the VC first Brillouin zone, the diffuse intensity determining the contrast of our images is contained in reciprocal space cubes with $\langle 100\rangle$-oriented sides of length a^{-1} and centered on the N systematic row reflections considered. This is a direct consequence of the rigid-ion approximation.[26] Moreover, when the diffuse distributions associated with the various reflections $\mathbf{g}$ do not overlap, which is the case here, $|\phi_{\mathbf{g}}(\mathbf{r})|^2$ can rightly be considered[26] as the intensity, at point $\mathbf{r}$ of the exit face of the crystal, in the dark-field image formed by placing an aperture around the $\mathbf{g}$ diffracted beam. Amongst all the possible $hk0$ reflections of the systematic row, we include strong ($h+k=4q$, q integer) and sometimes weak ($h+k=4q+2$) sphalerite reflections. Including reflections with $h+k=2q+1$, which are forbidden in the VC but whose associated cube contains some faint diffuse scattering, produced only very slight differences in the images.

Two methods were used to solve system (10). First, the crystal was divided in columns parallel to $\mathbf{Z}$, and (10) solved in all columns simultaneously by using the matrix method[10] supplemented by Newton's method for terms involving the partial derivatives in X and Y, which constitute the departure from the column approximation.[25] In each column and at each step along $\mathbf{Z}$, these derivatives were approximated by differences involving the values of $\phi_{\mathbf{g}}$ in the adjacent columns. The sampling intervals were typically a along $\mathbf{X}$ and $\mathbf{Y}$ and the computation steps $a/2$ along $\mathbf{Z}$. Finer grids did not produce substantial differences in the images.

A second method was used as a check for the images corresponding to $\mathbf{G}=p00$. All $(\mathbf{K}+\mathbf{g})_Y$ are then zero and we neglected the terms in $\partial^2\phi_{\mathbf{g}}/\partial Y^2$. Thanks to the PBC's, the X dependence of $\phi_{\mathbf{g}}$ was expressed as a Fourier series:

$$\phi_{\mathbf{g}}(X,Y,Z)=\sum_{m=0}^{N_X-1}\hat{\phi}^X_{\mathbf{g},m}(Y,Z)\exp(-2\pi imX/N_Xa)\ . \quad (11)$$

(10) could then be transformed into a system of $N\times N_X$ differential equations in Z governing the N_X Fourier components $\hat{\phi}^X_{\mathbf{g},m}(Y,Z)$, which was solved for fixed Y by using the standard one-dimensional Runge-Kutta routine D02BBF of the NAG library. The differences in the images were again slight.

The images were calculated up to the total thickness of the simulated specimens (132 nm), the intermediate results providing images for smaller thicknesses. Allowing for elastic relaxation at the free surfaces (see the end of Sec. II) altered the images very slightly only.

V. CALCULATED TEM IMAGES OF IDEALLY DISORDERED III-V CRYSTALLINE ALLOYS WITH ATOMIC SIZE EFFECT

The fundamental result of our simulations is that, because of the spatial correlations between the SD's, thin ideally disordered compositionally homogeneous crystals of III-V alloys with ASE's should display a strong CTEM contrast. We propose that this contrast be called atomic-size-effect contrast (ASEC). In this section, we describe this calculated contrast before discussing its origin in more detail in Sec. VI and comparing it with the experimental contrast in Sec. VII.

A. The calculated fine-scale contrast and its behavior upon changing diffraction conditions

The images of different ideally disordered specimens are, of course, different, but their statistical properties are similar. To illustrate this point, the figures which are not simulated images give the data corresponding to our full set of three large specimens. However, for the sake of clarity, all images, except in Fig. 3, are those of one particular simulated specimen under various diffraction conditions. Only in Fig. 3 do we compare the images of the three specimens in a given set of diffraction conditions. The particular specimen arbitrarily chosen for the rest of the images corresponds to Fig. 3(a). Several choices which had to be made as regards the calculation and display of the images will be justified at the end of Sec. V B in light of the results obtained. The contrast varies widely between the images discussed below. For clarity, we display all of them with an intensity scale running fully between black (low intensity) and white (high intensity), and we give in the caption or in the text their absolute contrast, defined as $(I_M-I_m)/(I_M+I_m)$, where I_M and I_m are the maximum and minimum image intensities.

As usual in CTEM, we discuss mainly images formed close to the Bragg condition for a given VC reflection $\mathbf{G}$.

(a) Bright-field and dark-field (DF) images both display a large contrast (Figs. 3–6).

(b) If $\mathbf{G}=400$, the contrast elements are elongated in the direction normal to $\mathbf{G}$ (Figs. 3 and 4). Consequently, the power spectra $J(k_X,k_Y)$ of the images (where k_X and k_Y are along reciprocal directions $\langle 100\rangle$ and $\langle 010\rangle$) are markedly anisotropic and their most intense parts are characteristically streaked along $\mathbf{G}$ (insets of Figs. 3 and 4).

(c) If $\mathbf{G}=220$, the contrast is more isotropic; some contrast elements are again elongated normally to $\mathbf{G}$, but many of its features are parallel to $\langle 100\rangle$ or $\langle 010\rangle$ (Fig. 5). Correlatively, the power spectra are now streaked along the [100] directions.

(d) More generally, there is no correlation between images of the same area corresponding to differently oriented $\mathbf{G}$ vectors. This applies for nonequivalent vectors

(e.g., 400 and 220), but also for equivalent ones [e.g., 400 and 040, which, according to result (b), produce two patterns elongated in perpendicular directions].

(e) The image is inverted when **G** is changed into $-\mathbf{G}$, for $w_G=0$.

(f) There is no correlation between images corresponding to substantially different primary beam kinetic energies E_0 [Fig. 6, to be compared with Fig. 3(a)].

(g) The contrast pattern of any area changes rapidly with w_G [Figs. 3(a) and 4]. Its scale diminishes when $|w_G|$ increases.

(h) More precisely, for $\mathbf{G}=400$, the power spectra of the images show that the contrast possesses a large range of wavelengths along **G** (insets in Figs. 3 and 4). For $w_G=0$, the traces across these spectra at $k_Y=0$ (Fig. 7) display a first peak for wavelengths around 10–15 nm. When $|w_G|$ increases, this peak remains, but the higher spatial frequencies are reinforced (Fig. 7).

(i) Weak-beam images (formed with $|w_G|$ large) show a strong contrast which is much finer and still definitely elongated normally to **G** [Fig. 8, to be compared with Figs. 3(a) and 4].

(j) The contrast amplitude $(I_M-I_m)/(I_M+I_m)$ oscillates with the specimen thickness t (Fig. 9). As expected, it is maximum when the average image intensity is least, namely, for DF images, when $t=n\xi_G^{\text{eff}}$, n integer, where $\xi_G^{\text{eff}}=\xi_G(1+w_G^2)^{-1/2}$ is the effective average extinction distance.[10]

(k) The characteristic contrast pattern only develops after the electron beam has traversed a certain thickness

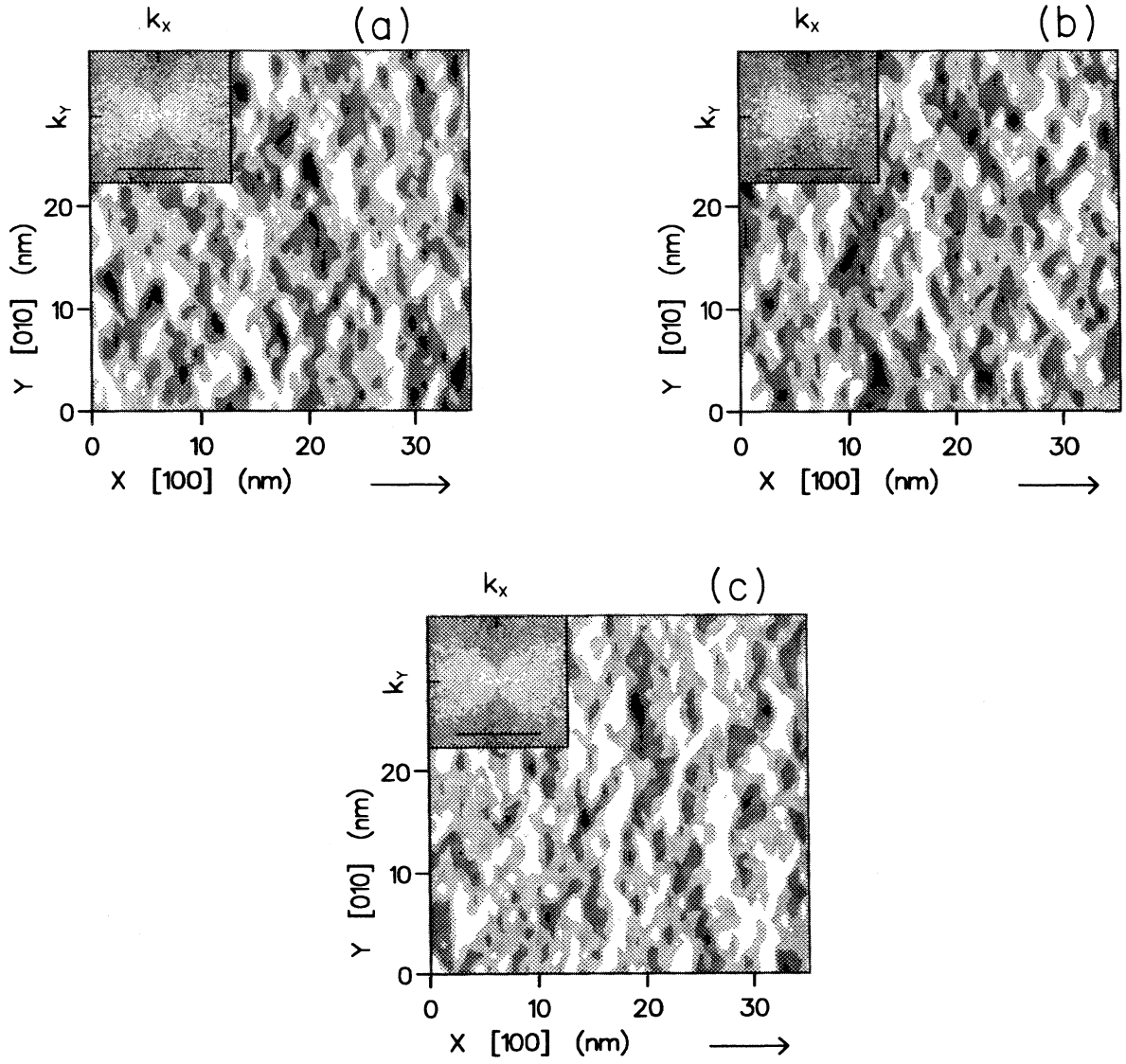

FIG. 3. Computed $\mathbf{G}=400$ dark-field TEM images of three compositionally homogeneous random $In_{0.5}Ga_{0.5}As$ specimens 132 nm thick, for $E_0=100$ keV, $w_{400}=0$, and $|u'_{400}/u_{400}|=0.2$. The arrow gives the direction of **G**. Image contrast is 0.43 (a), 0.40 (b), and 0.45 (c). In the power spectra $J(k_X,k_Y)$ of the images, given as insets, the bar corresponds to 1 nm^{-1}. All subsequent images, except Figs. 10 and 12, are from the specimen giving image (a) here (same area, same thickness).

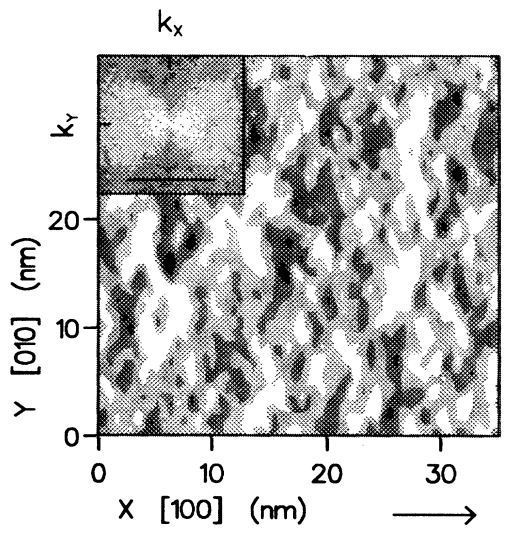

FIG. 4. Same as Fig. 3(a) for $w_{400}=1$ (image contrast = 0.74).

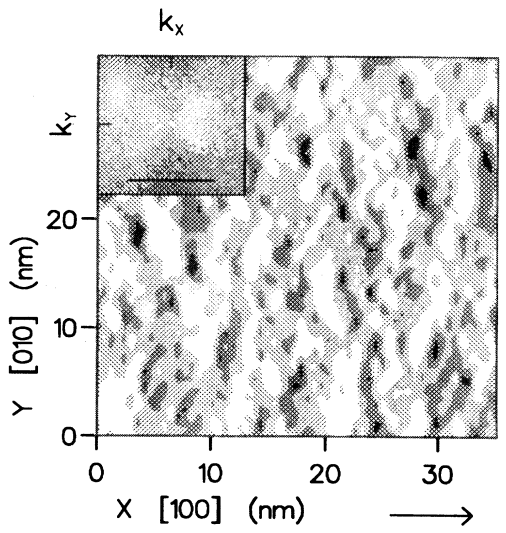

FIG. 6. Same as Fig. 3(a) for $E_0=200$ keV (image contrast = 0.19).

(about 35 nm for $\mathbf{G}=400$ at $w_{400}=0$). At lower specimen thicknesses, the contrast is not only very weak, but appears much finer and does not show any strong anisotropy (Fig. 10).

B. The effects of absorption and limited microscope resolution

Most parameters used in the simulations are known accurately. This is, however, not the case for the phenomenological absorption potential $u'_g(\mathbf{r})$. Its effect was thus investigated. The contrast pattern is remarkably insensitive to changes in the absorption parameters. Two quantities were varied independently: the ratios u'_0/u_0 and u'_g/u_g for $\mathbf{g}\neq\mathbf{0}$, taken as independent of $\mathbf{r}$ and $\mathbf{g}$, which describe, respectively, average and anomalous absorptions.[10] These parameters are often both taken equal to 0.1 in TEM simulations. Recent calculations suggest that u'_0/u_0 might be much lower and u'_g/u_g of this order for the materials and reflections considered here: according to Bird and King,[28] at 300 K and for $E_0=100$ keV, for GaAs and InAs, respectively, u'_0/u_0 is 0.03 and 0.05 and u'_{400}/u_{400} is 0.1 and 0.12. However, the contrast pattern

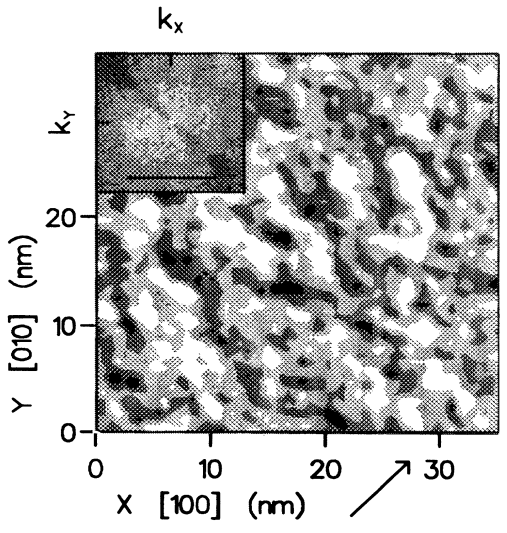

FIG. 5. Same as Fig. 3(a) for $\mathbf{G}=220$ and $w_{220}=0$ (image contrast = 0.32).

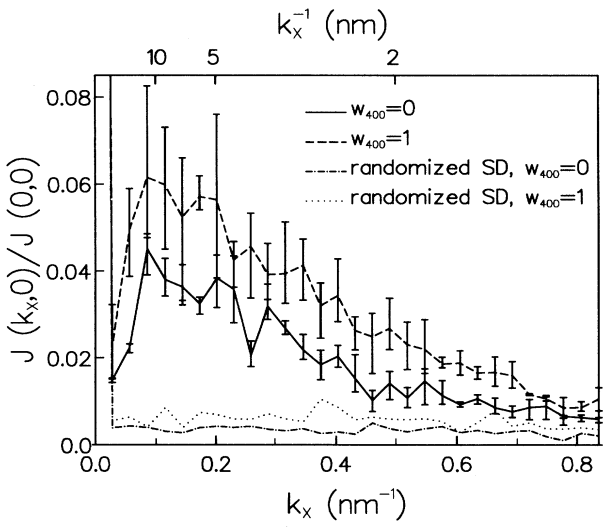

FIG. 7. Profiles along reciprocal direction $\langle 100\rangle$ at $k_Y=0$ of the power spectra $J(k_X,k_Y)$ of the 400 dark-field images computed for $w_{400}=0$ and $w_{400}=1$ for the three simulated specimens (curves: averages; segments: data spread; see Fig. 3) and for a specimen with randomized SD's (see Fig. 12 below). Normalizing by $J(0,0)$ amounts to equaling the average image intensities. The $k_Y=0$ values were obtained by averaging the spectra, for each k_X, in a narrow band of width $\Delta k_Y=0.14$ nm^{-1}.

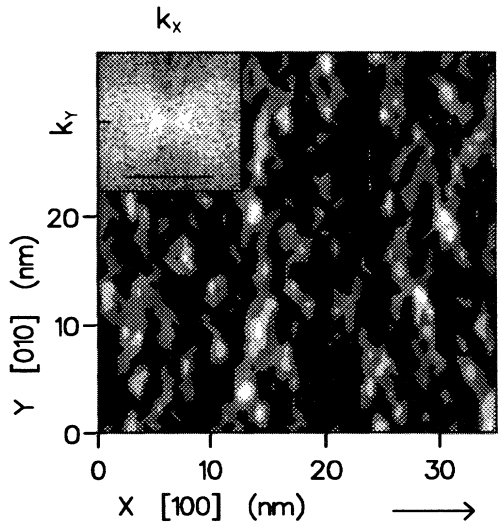

FIG. 8. Weak-beam image: same as Fig. 3(a) for $w_{400}=3$ (image contrast = 1).

and the contrast amplitude (but of course not the absolute image intensities) are totally insensitive to changes in u_0'/u_0. On the other hand, changes in anomalous absorption have two effects. First, if u_g'/u_g is very small (less than about 0.025), the contrast is much finer and isotropic, and thereby reminiscent of the contrast obtained at low thicknesses, but 0.025 is much less than the calculated values quoted above. Secondly, for higher values, the contrast amplitude decreases when u_g'/u_g increases but the contrast pattern remains very stable. A value of u_{400}'/u_{400} around 0.2 would seem to fit the experimental contrast best. This is shown in Fig. 9, whose experimental data are taken from Ref. 3, where the specimens studied were free from quasiperiodic composition modulations (for the relation between experimental and calculated fine contrast, see Sec. VII). In conclusion, including absorption is essential for obtaining the characteristic contrast, but, if not unrealistically low, the precise value of the absorption potential is irrelevant.

We also studied the effect on the images of the objective lens spherical aberration, of the size of the objective aperture, and of the energy spread of the primary beam. The previous results were not substantially altered. The contrast was slightly reduced, but the broad characteristic pattern of any given area remained unchanged, which is not surprising since all but the finest features of the contrast are coarser than the spatial resolution of a standard microscope operated in CTEM mode.

Finally, the images are only slightly modified if use is made of the column approximation instead of the Howie-Basinski equations.

The previous results justify the choices made for calculating and displaying the images.

(i) The images were calculated with the absorption parameters giving the best fit to the variation of the experimental fine contrast with thickness.[3]

(ii) Since the limitation in resolution of the microscope influences only slightly the images, all the results presented here were calculated without taking it into account.

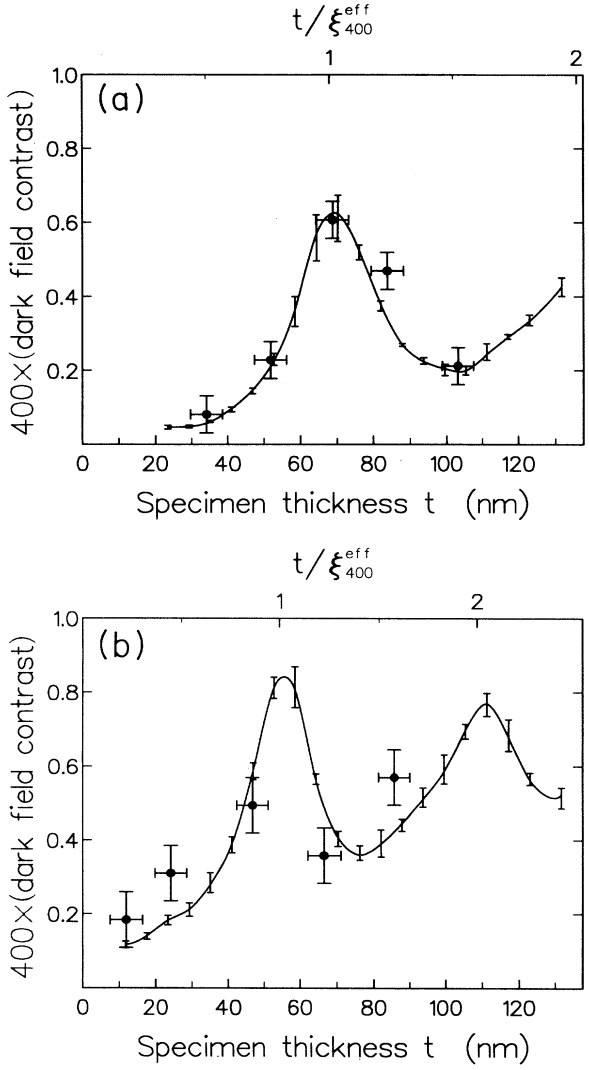

FIG. 9. Variation with specimen thickness of the fine 400 dark-field-image TEM contrasts calculated for compositionally homogeneous $In_{0.5}Ga_{0.5}As$ specimens (vertical segments and curve) and measured in $In_{0.53}Ga_{0.47}As$ specimens without coarse contrast (Ref. 3) (full circles), for (a) $w_{400}=0$ and (b) $w_{400}=0.75$. The segments give the spread of the data for the three simulated specimens, and the curves their averages. The contrast was computed for $E_0=100$ keV with $|u_0'/u_0|=0.1$ and $|u_{400}'/u_{400}|=0.2$.

VI. THE ORIGIN OF THE CHARACTERISTIC CONTRAST

A. The contrast is caused by the static atomic displacements

Both the behavior of the calculated contrast upon changing diffraction conditions, which strongly recalls that of the usual strain contrasts, and its scale, comparable with the ranges of the correlation functions calculated in Sec. III, suggest that it is indeed caused by the SD's. However, two related but distinct sources of contrast exist in such specimens: the presence of unlike atoms on the

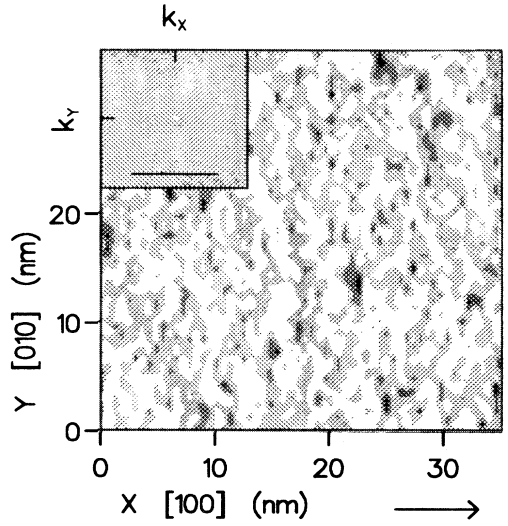

FIG. 10. Same as Fig. 3(a) for a specimen thickness of 18 nm (obtained by retaining only the corresponding upper part of the specimen) (image contrast = 0.05).

mixed sublattice(s) and the SD's. Both these sources are taken into account in our calculations, which make use of the rigid-ion approximation of the potential: Eq. (4) obviously accounts for both the different atomic potentials and the SD's. Nevertheless, the respective contributions to the total contrast of these two sources can be assessed. To this end, we used two methods. First, image simulations were performed on our specimens *before* VFF relaxation: the nature of the atom associated with any site of the mixed sublattice was kept the same, but all atoms were exactly at their VC sites. Only a faint contrast (0.08 for $\mathbf{G}=400$ and $t=132$ nm) remained, very different from the previous one [Fig. 11(a), to be compared with Fig. 3(a)]: it shows only a weak anisotropy (which does not appear in the equivalent images calculated within the column approximation, and is thus due to the breakdown of the latter) and its scale is much smaller (less than 2 nm). This is the residual purely "chemical" contrast caused by the fluctuations in the random distribution of scattering factors resulting from the random distribution of atoms on the mixed sublattice. Second, image simulations were performed again on the same specimens, retaining the calculated SD's, but the scattering factor f^q of any atom of the mixed sublattice was taken as the average, weighted according to the global composition ($x=0.5$ here) of those of Ga and In. The amplitude of the contrast was slightly reduced with respect to the full calculation (with both chemical and position disorders) but, except for the finest details, the contrast pattern was remarkably similar [Fig. 11(b), to be compared with Fig. 3(a)]. These two calculations prove unambiguously that the characteristic contrast is due to the SD's, not to the local fluctuations in the occupations of the sites of the mixed sublattice.

B. The contrast is caused by the spatial correlations between the static atomic displacements

A further calculation proves that the contrast results not merely from the SD's but from the *spatial correlations* between them. We simulated the images of the "randomized specimens" described in Sec. III, where the SD's are retained but permuted so that all their spatial correlations are destroyed. Once again, only a very fine nondirectional faint contrast (0.14 for $\mathbf{G}=400$ and $t=132$ nm) remained [Fig. 12, to be compared with Fig. 3(a)]. The power spectra of the images are flat and their intensity is low (Fig. 7).

In order to understand the calculated contrast, two

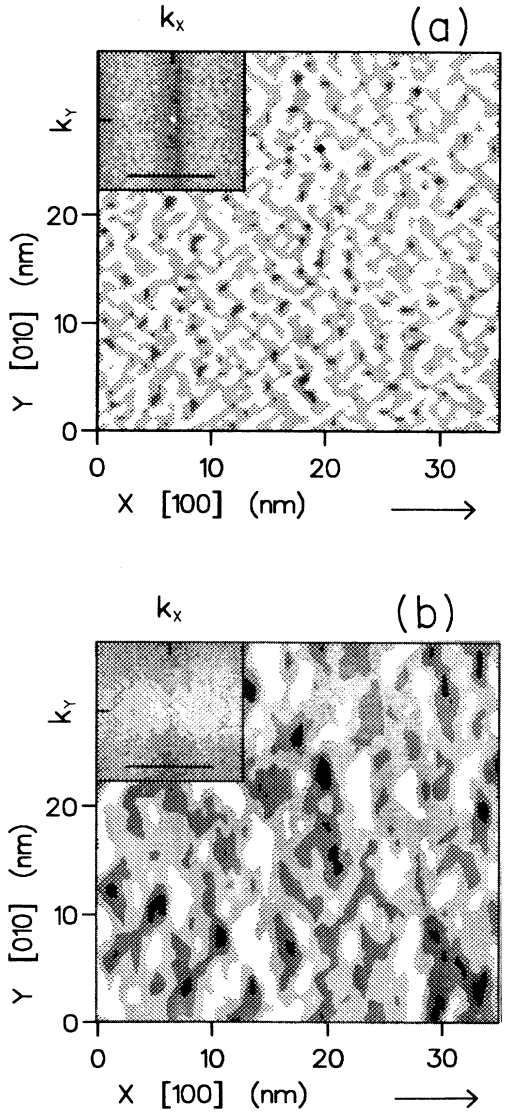

FIG. 11. 400 dark-field images of the specimen of Fig. 3(a) calculated (a) with zero static atomic displacements (image contrast = 0.08), and (b) with the same atomic scattering factors for Ga and In (image contrast = 0.35). The other parameters are the same as in Fig. 3(a).

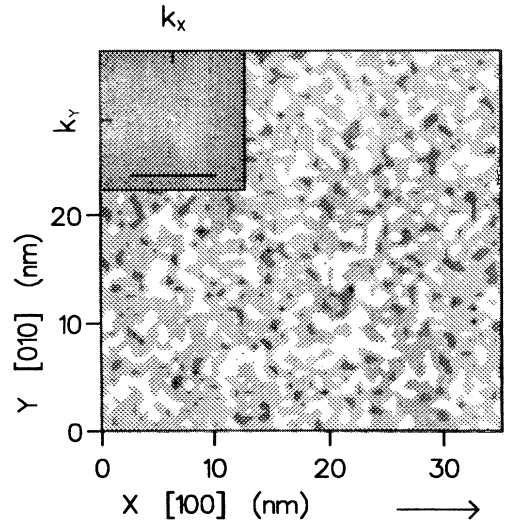

FIG. 12. 400 dark-field image of the specimen of Fig. 3(a) after randomization (i.e., with uncorrelated static atomic displacements). Each atom kept its own SD. The other parameters are the same as in Fig. 3(a) (image contrast = 0.14).

facts must thus be considered. First, as already noticed in the case of III-V alloys truly inhomogeneous in composition,[16,4] in the presence of both spatial variations of the scattering factors and strain, the CTEM contrast is usually dominated by the latter. This still holds in the present study, whose originality is of course that it proves that strain and the contrast induced are inevitable *even in compositionally homogeneous alloys.* Second, the fairly large characteristic scale of the contrast results from a difference between the correlation lengths of (i) the fluctuations of the occupations of the mixed sites by the two types of atoms (Ga and In) and (ii) the associated SD's. In our ideally disordered simulated crystals, the correlation length of the composition fluctuations is by definition zero. In contrast, and although they result from these totally uncorrelated composition fluctuations, the SD's are correlated over large distances, as shown in Sec. III. Moreover, the portion of the strain field associated with the locally averaged SD $\bar{\mathbf{R}}$ investigated at the end of Sec. III is very likely responsible for most of the contrast at scales of more than about 1 nm.

C. Discussion

Any strain can ultimately be described in terms of SD's. In that sense, the contrast studied here is a type of strain contrast, and indeed its behavior upon changing diffraction conditions (Sec. V A) is reminiscent in many ways of the usual strain contrast.[10] However, it differs not only from the latter, which is an image of the strain field induced by some kind of compositional or structural inhomogeneity (see Sec. I B), but also from the more subtle contrast arising from the SD's induced in a matrix by a low concentration of misfitting atomic impurities (or more generally point defects).[29–31] In the latter case, the TEM image is a map not of the strain field induced by the impurities, but of the changes in extinction and absorption distances caused by changes in the concentration of impurities. Consequently, no such contrast exists in a compositionally homogeneous area, at variance with the contrast studied here. In addition, if the impurity-induced SD's are isotropic, the images corresponding to equivalent **G** reflections are identical, which is not the case here [results (b)–(e) of Sec. V A]. All these differences result from the fact that the contrast investigated in Refs. 29–31 is in essence a structure-factor contrast (even if the changes in structure factor are caused by SD's), whilst our ASEC is a strain contrast. Ultimately, it results from the fact, demonstrated in Sec. III, that specimens homogeneous in composition nevertheless display a spatially varying strain field.

Since diffraction contrast is sensitive to weak strain fields, the CTEM images of *isolated* strain centers, such as inclusions or dislocations, which induce a long-range strain field, have a characteristic size usually much larger than these centers.[10] The same difference of scale is observed here, but no intuitive picture can be obtained unless correlation functions are used, since the long-range strain field is the complex result of the effect of all the atoms, each of which acts as a strain center by displacing all atoms in its vicinity, and is itself displaced by its neighbors. As usual, changing the diffraction conditions, either with [results (b)–(e)] or without [results (f)–(i) compared with result (b)] changing the diffraction vector, amounts to probing various wavelengths of this strain field.[4]

We of course expect such a contrast to exist, not only in all III-V alloys with ASE's (see Sec. II), but also in any alloy where the SD's are sufficiently large and correlated. We leave open the question of deciding if such spatial correlations of the SD's are a general feature of alloys with ASE's or if they produce here particularly noticeable effects because of the covalent nature of the material. The results of Butler, Withers, and Welberry[9] showing that the diffraction counterpart of these correlations (the diffuse planes in reciprocal space) exist for some oxide alloys, similarly to what we had previously demonstrated for the III-V alloys with ASE's,[3,5] suggest that the contrast induced by the SD's should exist for a much wider class of materials than the latter.

If the alloy is not ideally homogeneous in composition (and not perfectly ordered either), SD's with some degree of disorder will still exist, and the present contrast will be superimposed on the contrast induced by the proper composition inhomogeneities. In other words, the SD correlations will be partly intrinsic and partly due to the lack of compositional homogeneity. An important achievement would be to extract the contrast due to the genuine composition inhomogeneities from the total contrast in the TEM images of such specimens. Only in fully ordered alloys, where both the occupations and the SD's have perfectly periodic correlation functions, will the ASEC vanish.

VII. COMPARISON BETWEEN THE CALCULATED AND EXPERIMENTAL TEM FINE CONTRASTS IN III-V ALLOYS

All the experimental CTEM plan-view images of as-grown lattice-matched epitaxial layers of III-V alloys with ASE's display a characteristic contrast, usually called "fine contrast" (FC) to differentiate it from the "coarse contrast" (size ~ 150 nm) which arises undoubtedly from genuine quasiperiodic composition modulations.[12,16,4,32,33] Lattice-mismatched layers are known to be prone to composition variations developing during growth, which produce standard TEM contrasts; we do not consider them here. To our knowledge, there is no TEM study of bulk III-V alloys. The FC was reported by Roberts, Scott, and Gowers[11] and subsequently studied by many authors.[3,4,12–18] It clearly behaves as a strain contrast.[3,4] In line with the assumption discussed in Sec. I B, most authors have concluded from the observation of the FC that all such layers are compositionally inhomogeneous. However, we suggested early on[4] that the FC might be caused not by proper composition inhomogeneities, i.e., statistically significant deviations from the mere fluctuations of composition expected in any alloy (unless it is perfectly ordered), but simply by the SD's present even in the ideally homogeneous alloys.

Indeed, doubts arise for several reasons.

(i) There is no other proof that composition inhomogeneities of a scale less than or equal to that of the FC systematically exist in these lattice-matched layers. Electron-beam microanalysis never detected such small-scale composition variations.[4] The anisotropic diffuse features observed in the diffraction patterns[3] have been shown to be compatible with a compositional homogeneity of the alloy.[5] The pulse laser atom probe experiments of Mackenzie, Liddle, and Grovenor detected statistically significant clustering in some specimens, none in others, although the FC was present in all.[34] EXAFS detects no clustering.[35] Finally, a recent scanning tunneling microscopy study concludes that the group-V atoms are randomly distributed in $In_{0.25}Ga_{0.75}As_{0.5}P_{0.5}$ layers lattice matched to InP.[36]

(ii) The FC changes with diffraction conditions,[3,4] so that it is impossible to associate its features with spatially well-defined composition inhomogeneities.

(iii) The FC exists in any layer, irrespective of its technique and conditions of fabrication. It seems to have always the same aspect and to behave in the same way upon changing diffraction conditions.

On the other hand, if the FC was intrinsic to the III-V alloys with ASE's, it should also appear in the CTEM cross-sectional images of these epitaxial layers. However, these images usually display features elongated along the [001] growth direction and whose contrast disappears in the $\mathbf{G}=004$ images,[37] which might be indicative of genuine composition modulations in directions parallel to the substrate surface. Although it is often assumed that this contrast and the FC share the same origin, no definite relation has yet been established between them. Moreover, the published data[37,18,38] seem to display this cross-sectional contrast only in layers grown under conditions where the quasiperiodic composition modulations appear.[4] Cross sections of specimens devoid of such modulations[18] show a contrast more reminiscent of the FC observed in plan-view images. The columnar contrast might thus be associated with the coarse quasiperiodic contrast and not with the FC.

Thanks to the present calculations, these controversial questions may now be discussed more soundly. All but maybe one of the characteristic features of the computed contrast listed in Sec. V A have unambiguously been reported as experimental observations upon the FC by either all or most authors [features (a)–(d) (Refs. 3,4,12–18)] or at least in some detailed studies [features (e),[3,16,18] (f),[32] (g),[3,4] (i),[16,4,39] (j),[3,32] and (k)[3,16,18,32]].

The only feature which might differentiate the experimental and calculated contrasts is their apparent sizes. Up until recently, the characteristic size of the FC, defined as its average repeat distance along [400] in the $\mathbf{G}=400$ images taken with $w_{400}=0$ (recall that the FC size changes rapidly with the deviation parameter), seemed to lie always between 10 and 15 nm (with possibly small differences between alloys[13]) and not to depend on the method and conditions of growth. Our calculated images seem to indicate a prominent size of the order of 5 nm. However, the experimental and calculated contrasts both display a considerable range of spatial wavelengths. Gowers[13] reports a lowest spatial frequency of 6 nm in $In_{0.54}Ga_{0.46}As$, and McDevitt *et al.*,[38] who have published power spectra (optical diffractograms) of their experimental images, report the presence of diffuse intensity along the direction of **G**. The mere examination of the experimental micrographs shows that no well-defined wavelength can be attributed to the FC. On the other hand, the power spectra of our calculated images (Figs. 3 and 7) display some long wavelengths, around 10 nm [result (h)]. Since these are of the order of a third of the size of our supercells, and since any area examined in a typical experimental micrograph is much larger than our calculated images, these long wavelengths are likely to be more visible in the experiments than in our simulations.

However, the similarity of behaviors of the experimental and calculated contrasts is not in itself a proof that they are one and the same thing. The question is further complicated by recent observations. McDevitt *et al.*[38] reported a contrast finer (~ 5–6 nm) than the usual FC in some layers as well as an increase of its size with the growth temperature, and Seong, Booker, and Norman[39] have observed the coexistence of the FC and of a finer contrast (size ~ 5 nm). In addition, annealing experiments demonstrated an evolution of the size of the FC which had not been observed in the early experiments of Launois *et al.*:[40] McDevitt *et al.*[41] and Seong, Booker, and Norman[39] reported that only the new contrast, which could be called "very fine" (VFC), remains after sufficient annealing. Its behavior upon changing diffraction conditions is again identical to that of the usual FC and of our calculated contrast. Indeed, the identity between the VFC and our calculated contrast extends to their prominent sizes (as long as we content ourselves with the present size of our simulated specimens; see above). To reach a final decision as regards the composi-

tional homogeneity of the as-grown layers, one should probably simulate the TEM images of even larger specimens and compare the power spectra of the experimental and calculated images. TEM images of cross-sectional specimens without coarse contrast in plan view and of bulk III-V alloys would also be welcomed.

In conclusion, the origin of the FC remains unclear, since some experiments tend to associate it with genuine composition variations, whilst others do not. One possibility is that there could exist two kinds of fine contrasts, the usual FC possibly due to proper composition variations (albeit on a scale and with an amplitude which remains to be determined) and the recently reported VFC, intrinsic because it would exist even in alloys perfectly homogeneous in composition. This justifies our previous suggestion[4] and might reconcile the two opposed views held up to now upon the sources of fine contrast in these alloys. Nevertheless, a conclusion emerges from both experiment and calculations: a considerable fine-scale contrast exists in the TEM images of all the layers of any III-V alloy with ASE's, even when they are ideally homogeneous in composition, unless the alloy is perfectly ordered. Even if the absence of the usual FC in some as-grown and annealed layers was confirmed, the necessity to disentangle the contrast here calculated, caused by the SD's, from the contrast due to proper composition inhomogeneities, and the question of the relationship between the spectral characteristics of these inhomogeneities and of the contrast, would remain. Only image calculations such as the present ones, taking fully into account the inevitable correlated SD's, will qualify to answer these questions.

VIII. CONCLUSIONS

We demonstrated by performing dynamical image calculations that considerable contrast may exist in the TEM micrographs of crystalline alloys displaying an atomic size effect. This contrast is due to the spatial correlations of the static atomic displacements from the sites of the average lattice of the alloy. These correlations and the contrast exist even if the alloy is fully disordered. Consequently, and contrary to what is often assumed, the observation of some contrast in TEM does not imply that the specimen examined is truly inhomogeneous in composition. In the particular case of III-V alloys, we gave the values of the main correlation functions of the static atomic displacements and we computed micrographs of ideally homogeneous alloys under a wide range of diffraction conditions. The calculations reproduce well the behavior of the fine-scale contrast observed in the experimental TEM images of these alloys.

ACKNOWLEDGMENTS

We thank B. Jouffrey and V. Barnole for many stimulating discussions. Years of scientific conversations with Pierre Hénoc are gratefully remembered.

[1]B. E. Warren, B. L. Averbach, and B. W. Roberts, J. Appl. Phys. **22**, 1493 (1951).

[2]B. Borie and G. J. Sparks, Jr., Acta Crystallogr. Sect. A **27**, 198 (1971).

[3]F. Glas, P. Hénoc, and H. Launois, in *Microscopy of Semiconducting Materials 1985,* edited by A. G. Cullis and D. B. Holt, IOP Conf. Proc. No. 76 (Institute of Physics, Bristol, 1985), pp. 251–256.

[4]F. Glas, in *Evaluation of Advanced Semiconductor Materials by Electron Microscopy,* edited by D. Cherns, NATO Advanced Study Institute Series B: Physics Vol. 203 (Plenum, New York, 1989), pp. 217–232.

[5]F. Glas, C. Gors, and P. Hénoc, Philos. Mag. B **62**, 373 (1990).

[6]P. N. Keating, Phys. Rev. **145**, 637 (1966).

[7]R. M. Martin, Phys. Rev. B **1**, 4005 (1970).

[8]M. Podgórny, M. T. Czyzyk, A. Balzarotti, P. Letardi, A. Kisiel, and M. Zimnal-Starnawska, Solid State Commun. **55**, 413 (1985).

[9]B. D. Butler, R. L. Withers, and T. R. Welberry, Acta Crystallogr. Sect. A **48**, 737 (1992).

[10]P. B. Hirsch, A. Howie, R. B. Nicholson, D. W. Pashley, and M. J. Whelan, *Electron Microscopy of Thin Crystals* (Krieger, Malabar, 1977), pp. 199, 202, 216, 218, 248–253, 276, 289–291, 327–337.

[11]J. S. Roberts, G. B. Scott, and J. P. Gowers, J. Appl. Phys. **52**, 4018 (1981).

[12]P. Hénoc, A. Izrael, M. Quillec, and H. Launois, Appl. Phys. Lett. **40**, 963 (1982).

[13]J. P. Gowers, Appl. Phys. A **31**, 23 (1983).

[14]F. Glas, M. M. J. Treacy, M. Quillec, and H. Launois, J. Phys. (Paris) Colloq. **43**, C5-11 (1982).

[15]S. Mahajan, B. V. Dutt, H. Temkin, R. J. Cava, and W. A. Bonner, J. Cryst. Growth **68**, 589 (1984).

[16]M. M. J. Treacy, J. M. Gibson, and A. Howie, Philos. Mag. A **51**, 389 (1985).

[17]A. G. Norman and G. R. Booker, J. Appl. Phys. **57**, 4715 (1985).

[18]A. J. Bons, Y. S. Oei, and F. W. Schapink, in *Microscopy of Semiconducting Materials 1989,* edited by A. G. Cullis and J. L. Hutchison, IOP Conf. Proc. No. 100 (Institute of Physics, Bristol, 1989), pp. 161–166.

[19]D. E. Laughlin, R. Sinclair, and L. E. Tanner, Scr. Metall. **14**, 373 (1980).

[20]J. C. Phillips, *Bonds and Bands in Semiconductors* (Academic, New York, 1973), pp. 13,20–22,212–214.

[21]J. C. Mikkelsen, Jr., and J. B. Boyce, Phys. Rev. B **28**, 7130 (1983).

[22]J. Bellessa, C. Gors, P. Launois, M. Quillec, and H. Launois, in *GaAs and Related Compounds 1982,* edited by G. E. Stillman, IOP Conf. Proc. No. 65 (Institute of Physics, Bristol, 1983), pp. 529–536.

[23]A. Marbeuf, F. Karouta, H. Dexpert, P. Lagarde, and A. Joullié, J. Phys. (Paris) Colloq. **47**, C8-369 (1986); T. Sasaki, T. Onda, R. Ito, and N. Ogasawara, Jpn. J. Appl. Phys. **25**, 231 (1986); H. Oyanagi, Y. Takeda, T. Matsushita, T. Ishiguro, and A. Sasaki, in *GaAs and Related Compounds 1985,* edited by M. Fujimoto, IOP Conf. Proc. No. 79 (Hilger, Bristol, 1986), pp. 295–300.

[24]F. Glas and P. Hénoc, Philos. Mag. A **56**, 311 (1987).

[25]A. Howie and Z. S. Basinski, Philos. Mag. **17**, 1039 (1968).

[26]G. R. Anstis and D. J. H. Cockayne, Acta Crystallogr. Sect. A **35**, 511 (1979).
[27]P. A. Doyle and P. S. Turner, Acta Crystallogr. Sect. A **24**, 390 (1968).
[28]D. M. Bird and Q. A. King, Acta Crystallogr. Sect. A **46**, 202 (1990).
[29]C. R. Hall, P. B. Hirsch, and G. R. Booker, Philos. Mag. **14**, 979 (1967).
[30]M. M. J. Treacy, J. M. Gibson, K. T. Short, and S. B. Rice, Ultramicroscopy **26**, 133 (1988).
[31]D. D. Perovic, G. C. Weatherly, R. F. Egerton, D. C. Houghton, and T. E. Jackman, Philos. Mag. A **63**, 757 (1991).
[32]F. Glas, in *Microscopy of Semiconducting Materials 1993,* edited by A. G. Cullis, A. E. Staton-Bevan and J. L. Hutchison, IOP Conf. Proc. No. 134 (Institute of Physics, Bristol, 1993), pp. 269–278.
[33]D. Cherns, P. D. Greene, A. Hainsworth, and A. R. Preston, in *Microscopy of Semiconducting Materials 1987,* edited by A. G. Cullis and P. D. Augustus, IOP Conf. Proc. No. 87 (Institute of Physics, Bristol, 1987), pp. 83–87.
[34]R. A. D. Mackenzie, J. A. Liddle, and C. R. M. Grovenor, J. Appl. Phys. **69**, 250 (1991).
[35]Y. Takeda, H. Oyanagi, and A. Sasaki, J. Appl. Phys. **68**, 4513 (1990).
[36]H. W. M. Salemink and O. Albrektsen, Phys. Rev. B **47**, 16 044 (1993).
[37]A. G. Norman and G. R. Booker, in *Microscopy of Semiconducting Materials 1985* (Ref. 3), pp. 257–262.
[38]T. L. McDevitt, S. Mahajan, D. E. Laughlin, W. A. Bonner, and V. G. Keramidas, Phys. Rev. B **45**, 6614 (1992).
[39]T. -Y. Seong, G. R. Booker, and A. G. Norman, in *Microscopy of Semiconducting Materials 1993* (Ref. 32), pp. 301–304.
[40]H. Launois, M. Quillec, F. Glas, and M. J. Treacy, in *GaAs and Related Compounds 1982* (Ref. 22), pp. 537–544.
[41]T. L. McDevitt, S. Mahajan, D. E. Laughlin, W. A. Bonner, and V. G. Keramidas, in *Microscopy of Semiconducting Materials 1991,* edited by A. G. Cullis and N. J. Long, IOP Conf. Proc. No. 117, (Institute of Physics, Bristol, 1991), pp. 477–483.

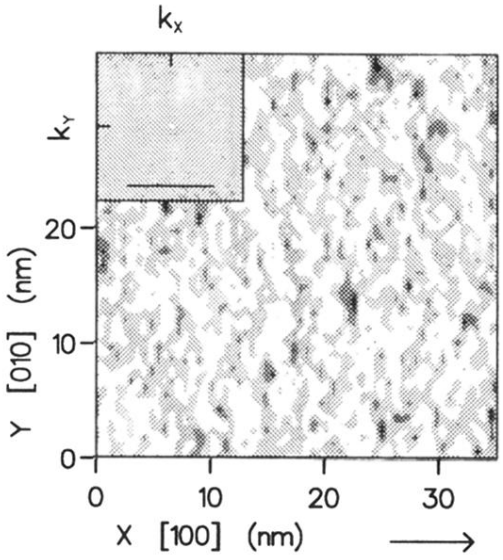

FIG. 10. Same as Fig. 3(a) for a specimen thickness of 18 nm (obtained by retaining only the corresponding upper part of the specimen) (image contrast = 0.05).

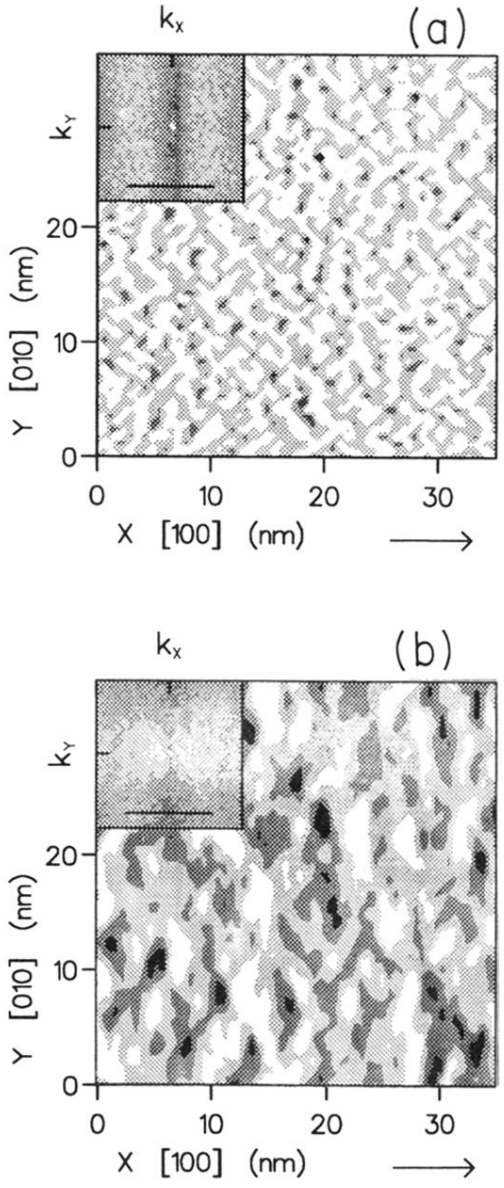

FIG. 11. 400 dark-field images of the specimen of Fig. 3(a) calculated (a) with zero static atomic displacements (image contrast = 0.08), and (b) with the same atomic scattering factors for Ga and In (image contrast = 0.35). The other parameters are the same as in Fig. 3(a).

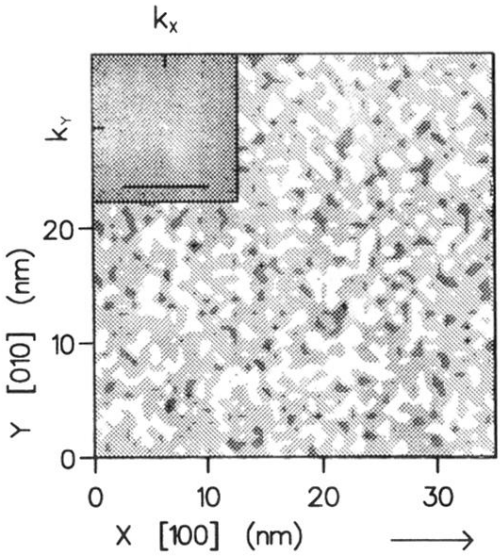

FIG. 12. 400 dark-field image of the specimen of Fig. 3(a) after randomization (i.e., with uncorrelated static atomic displacements). Each atom kept its own SD. The other parameters are the same as in Fig. 3(a) (image contrast = 0.14).

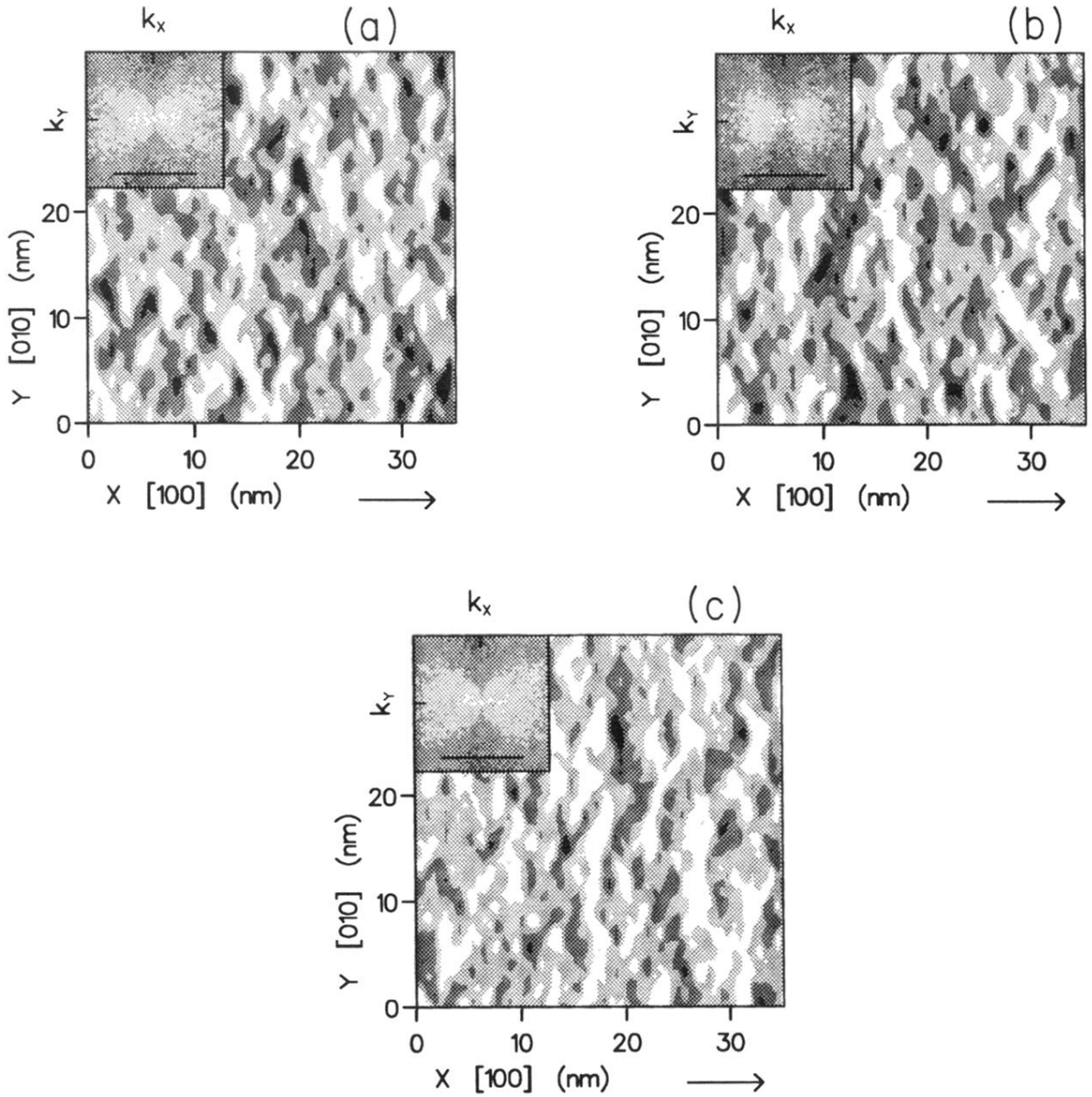

FIG. 3. Computed $\mathbf{G}=400$ dark-field TEM images of three compositionally homogeneous random $In_{0.5}Ga_{0.5}As$ specimens 132 nm thick, for $E_0=100$ keV, $w_{400}=0$, and $|u'_{400}/u_{400}|=0.2$. The arrow gives the direction of $\mathbf{G}$. Image contrast is 0.43 (a), 0.40 (b), and 0.45 (c). In the power spectra $J(k_X,k_Y)$ of the images, given as insets, the bar corresponds to 1 nm^{-1}. All subsequent images, except Figs. 10 and 12, are from the specimen giving image (a) here (same area, same thickness).

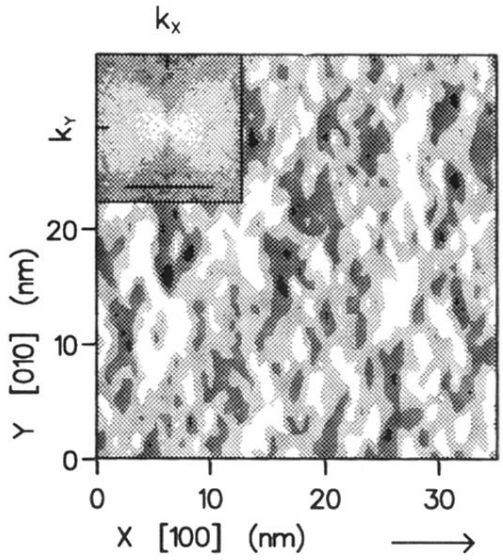

FIG. 4. Same as Fig. 3(a) for $w_{400}=1$ (image contrast = 0.74).

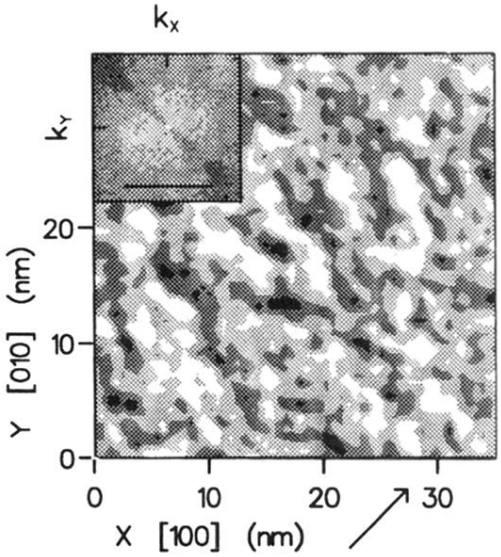

FIG. 5. Same as Fig. 3(a) for $\mathbf{G}=220$ and $w_{220}=0$ (image contrast = 0.32).

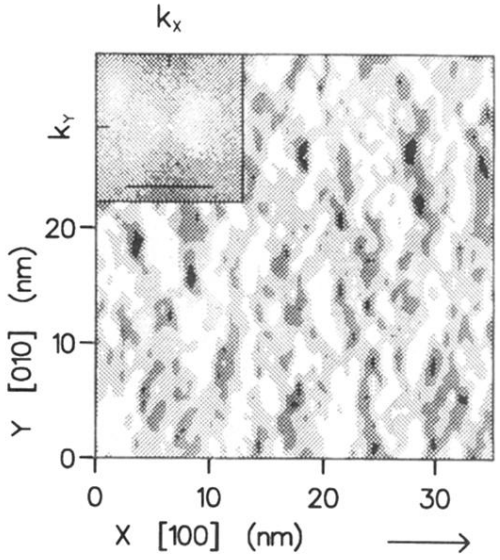

FIG. 6. Same as Fig. 3(a) for $E_0 = 200$ keV (image contrast = 0.19).

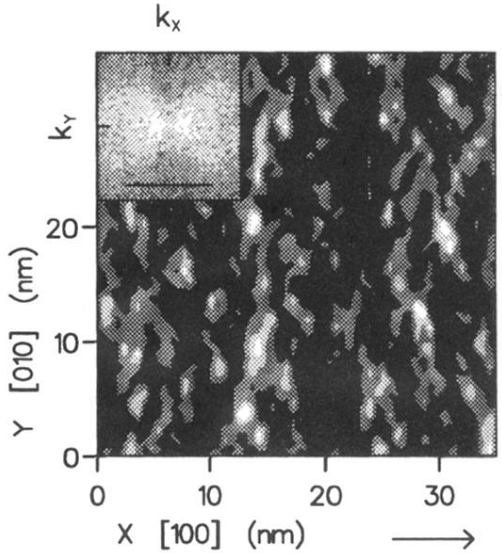

FIG. 8. Weak-beam image: same as Fig. 3(a) for $w_{400} = 3$ (image contrast = 1).